



Microstructural Development in Inconel 718 Nickel-Based Superalloy Additively Manufactured by Laser Powder Bed Fusion

Thinh Huynh¹ · Abhishek Mehta¹ · Kevin Graydon¹ · Jeongmin Woo¹ · Sharon Park^{1,3} · Holden Hyer^{1,4} · Le Zhou^{1,5} · D. Devin Imholte² · Nicolas E. Woolstenhulme² · Daniel M. Wachs² · Yongho Sohn¹

Received: 10 November 2021 / Accepted: 18 November 2021 / Published online: 10 January 2022
© ASM International 2021

Abstract

Excellent weldability and high temperature stability make Inconel 718 (IN718) one of the most popular alloys to be produced by additive manufacturing. In this study, we investigated the effects of laser powder bed fusion (LPBF) parameters on the microstructure and relative density of IN718. The samples were fabricated with independently varied laser power (125–350 W), laser scan speed (200–2200 mm/s), and laser scan rotation (0°–90°). Archimedes' method, optical microscopy, and scanning electron microscopy were employed to assess the influence of LPBF parameters on the relative density and microstructure. Optimal processing windows were identified for a wide range of processing parameters, and relative density greater than 99.5% was achieved using volumetric energy density between 50 and 100 J/mm³. Microstructural features including melt pool geometry, lack of fusion defect, keyhole porosity, and sub-grain cellular microstructure were examined and quantified to correlate to LPBF parameters. A simple empirical model was postulated to relate relative sample density and LPBF volumetric energy density. Melt pool dimensions were quantitatively measured and compared to estimations based on Rosenthal solution, which yielded a good agreement with the width, but underestimated the depth, particularly at high energy input, due to lack of consideration for keyhole mode. In addition, the sub-grain cellular-dendritic microstructure in the as-built samples was observed to decrease with increasing laser scan speed. Quantification of the sub-micron cellular-dendritic microstructure yielded estimated cooling rate in the order of 10⁵–10⁷ K/s.

Keywords Additive manufacturing · Microstructure · Quantitative metallography · Superalloys · Solidification

Introduction

Laser powder bed fusion (LPBF), also known as selective laser melting (SLM), utilizes laser to melt selective regions of a powder bed, layer-by-layer, corresponding to

the sliced model of a computer-generated design. Since the rapid movement of the laser is accompanied by a very rapid solidification/cooling (10³–10⁸ K/s) [1, 2], nearly unlimited geometrical complexity and customization can be adopted to produce near-net-shape components.

Traditional manufacturing techniques such as casting, forging, and powder metallurgy have been established for manufacturing of Inconel 718 (IN718) [3, 4]. However, recent advancements in metal additive manufacturing (AM) enabled rapid production of complex geometries while providing design freedom for customized components [5, 6]. Since it is impractical to work harden components produced via LPBF, precipitation strengthened alloys such as IN718 received spotlights in AM technologies. While rapid solidification [7–9] and directional cooling [10–12] influence the as-built microstructure [13–16] and phase transformations [17–19], repeated thermal cycling adds another layer of complexity. Extreme cooling rates as high as 10⁸ K/s can induce constitutional supercooling ahead of the solidification front, which result in the instability of the solid–liquid

✉ Yongho Sohn
yongho.sohn@ucf.edu

¹ Department of Materials Science and Engineering, Advanced Materials Processing and Analysis Center, University of Central Florida, Orlando, FL 32816, USA

² Nuclear Fuels and Materials Division, Idaho National Laboratory, Idaho Falls, ID 83415, USA

³ Present Address: Department of Materials Science and Engineering, Johns Hopkins University, Baltimore, MD, USA

⁴ Present Address: Oak Ridge National Laboratory, Oak Ridge, TN 37830, USA

⁵ Present Address: Department of Mechanical Engineering, Marquette University, Milwaukee, WI 53233, USA

interface [20, 21]. Consequently, the non-planar solidification will assume cellular or dendritic morphologies [22]. The as-printed microstructure of IN718 consists of a matrix of fine cellular dendrites [23–25]. Simulations mimicking solidification conditions of IN718 showed segregation of strengthening elements along the intercellular or interdendritic regions [26].

Based on transmission electron microscopy, Zhou et al. [27] demonstrated that the as-built microstructure was dominated by segregation of niobium (Nb), molybdenum (Mo), and titanium (Ti) along the cellular boundaries and interdendritic regions. Moreover, nano-scaled Laves in the form of $(\text{Ni,Cr,Fe})_2(\text{Nb,Mo,Ti})$ and carbides including $(\text{Nb,Ti})(\text{C,B})$ at 100–200 nm, and 50 nm, respectively, were observed in the as-built condition along the interdendritic regions with significant microsegregation. This is similar to that observed in a greater magnitude for wrought and cast material [28].

Over the past decade, researchers have focused on many aspects of microstructure and mechanical performance of IN718 [29–36]. Optimizing the processing parameters of LPBF can be quite arduous. Generally, the most influential processing parameters include laser power, laser scan speed, laser hatch spacing, and slice thickness. To understand the influence of these processing parameters on the relative density and microstructure, a normalized volumetric energy density can be adopted [1, 2] and is defined as:

$$\text{Energy Density(ED)} = \frac{\text{Laser Power}}{\text{Laser Scan Speed} \times \text{Hatch Spacing} \times \text{Slice Thickness}} \quad (1)$$

Despite numerous studies on this nickel-base superalloy, limited efforts were made to comprehensively document the influence of processing parameters. The mechanical properties of AM'ed IN718 have been widely explored in the literature, and a previous publication [27] detailing the correlation between microstructure and mechanical properties was completed. Thus, it is imperative to investigate how the variation in LPBF parameters can influence IN718 microstructure manufactured by LPBF. This work was carried out to correlate the LPBF parameters of IN718 with the relative density and microstructure. Estimation of cooling rates was also carried out using simple models available for solidification microstructure, and traditional welding to establish the trend between cooling rates and LPBF parameters.

Materials and Methods

Powder Characterization

Commercial IN718 powder feedstock for the LPBF was procured from SLM Solutions Group AG (Lubeck, Germany)

with the average particle diameter of 45 μm . The particle size distribution was further examined using laser diffraction particle size analyzer (Beckman Coulter LSTM 13 320). Powder morphology and microstructure were observed using a field emission scanning electron microscope (FE-SEM, Zeiss Ultra-55TM). As-received powders were mounted in epoxy resin and metallographically polished down to 0.25 μm diamond paste and etched using a mixed acid etchant for cross-sectional analysis. The etchant consisted of hydrochloric acid (HCl), acetic acid (CH_3COOH), and nitric acids (HN O_3) at a volumetric ratio of 3:2:1, respectively. Powder circularity and cross section microstructure were examined using optical microscope (Nikon Metaphot) and SEM, respectively. Chemical composition analysis of the powders was conducted using x-ray energy-dispersive spectroscopy (EDS) equipped on FE-SEM and compared to the chemistry standard ASTM F3055-14 reported in Table 1. Quantification of individual/overall powder density was carried out using image processing and analysis software (ImageJTM, NIH) from ten randomly selected areas.

Laser Powder Bed Fusion and Specimen Preparation

An SLM 125^{HL} (SLM Solutions Group AG Lubeck, Germany) LPBF system, equipped with a single continuous-wave (1070 nm) IPG fiber laser, was employed to print cubic

samples with dimensions of 10 x 10 x 10 mm. All samples were fabricated on an IN718 substrate pre-heated to 100 °C and within an argon atmosphere containing an oxygen content below 0.1 %. The most influential processing parameters including laser power, laser scan speed, and laser scan rotation were varied independently to examine the formation of defects and microstructure. The processing parameters were varied systematically around the optimized parameter set obtained from SLM Solutions specifications in which the laser power, scan speed, slice thickness, hatch spacing, and scan rotation angle are 200 W, 900 mm/s, 0.03 mm, 0.12 mm, and 16°, respectively.

In order to observe the melt pool characteristics in LPBF, initial layer rotation was adjusted to ensure that the last melt pool is perpendicular to the XZ plane. After fabrication, the samples were removed from the substrate *without* standard stress relieving (ASTM F3055). Lateral and bottom surfaces of the samples were ground using silicon carbide (SiC) paper to minimize surface bubbles during density measurements via immersion technique. Relative density measurements of the printed samples were conducted via Archimedes' method, pursuant of ASTM B962 - 17. The

Table 1 Composition (wt.%) of IN718 powder feedstock from EDS and ASTM F3055 - 14

	Ni	Cr	Fe	Nb	Mo	Co	Ti	Al	Si	Mn
EDS	51.3 (± 0.59)	20.4 (± 0.18)	18.9 (± 0.59)	4.6 (± 0.59)	2.5 (± 0.21)	0.1 (± 0.17)	1.0 (± 0.16)	1.0 (± 0.20)	0.2 (± 0.09)	0.1 (± 0.09)
ASTM	50.0–55.0	17.0–21.0	17.0	4.75–5.5	2.8–3.3	1.00	0.65–1.15	0.20–0.80	0.35	0.35

samples were cross sectioned parallel to the build direction (XZ) and perpendicular to the build direction (XY), with the z-axis along the build direction. All sample surfaces were metallographically polished down to 0.25 μm diamond paste using standard metallographic procedures and etched using the above-mentioned etchant for 30–60 sec.

Microstructural Characterization

Microstructures before and after chemical etching were examined using optical microscopy and SEM, respectively. Prior to etching, the porosity in each sample was quantified via image analysis, and the average relative density was estimated by assuming the area fraction of defects was equal to the volume fraction. To ensure statistical confidence, relative density was determined using 10 optical micrographs at 50X magnification. After chemical etching, the melt pool depth and width of the last melted layer (e.g., top of the sample) for each sample were obtained via image analysis. Melt pool dimensions were acquired using the measurement technique illustrated in Fig. 1. Assuming parabolic symmetry, the actual melt pool widths were approximated to be twice the measured width. Statistical variation in the melt pool dimensions was estimated using 5 random optical micrographs at 50X magnification. Quantification of the cellular microstructure using the linear intercept method, pursuant of ASTM E112-13, was conducted via image analysis. Chemical composition of the segregated microstructure was obtained using EDS on FE-SEM.

Results and Discussion

Powder Feedstock Morphology and Microstructure

Typical composition of IN718 powders is reported in Table 1. Figure 2 presents that the mean particle size of the powder feedstock was 32.90 μm , and 90 percent of the distribution lied below 44.26 μm . Cross-sectional optical micrograph of IN718 powders, presented in Fig. 3(a), demonstrates that the powders were highly circular with negligible internal porosity. Quantification of the powder circularity and powder density yielded 0.88 ± 0.01 and $99.98 \pm 0.02\%$,

respectively. Figure 3(b) illustrates the overall spherical nature of the powders with limited satellite formation around the powder surface. The backscatter electron (BSE) images in Fig. 3(c) and (d) indicates elemental contrast of the dendritic microstructure. Compositional analysis reported in Table 2 suggested that the cellular boundaries (point 2) to be enriched in Nb, Ti, and Mo as compared to the primary γ matrix (point 1).

Effect of Laser Power and Scan Speed on Defect Formation

To explore the effects of laser power and laser scan speed on the relative density of IN718 samples, optical micrographs were utilized for image analysis to estimate the sample density over a wide range combinations of laser powers and laser scan speeds. As shown in Fig. 4, samples with slow laser scan speeds had mostly circular porosity induced by keyhole melting. As the laser scan speed increased, a clear departure from circular pores was observed. At a constant laser power, an increase in laser scan speed was accompanied with a transition from low-density to high-density samples. When the laser scan speed exceeded the high-density threshold, a lower density microstructure appeared with irregularly shaped lack of fusion flaws. While the transition of defect formation characteristic remained similar across all investigated laser powers, samples fabricated with higher laser powers had more gradual transitions from low-density to high-density regions. In other words, the LPBF processing window that produced higher relative density for IN718 was observed to be larger when fabricated with 275 W and 350 W. The overall trend in sample density (or pores/flaws) is presented in Fig. 5 as functions of laser power and scan speed.

Optical micrographs in Figs. 4 and 5 clearly display the transition from circular pores to high part density, and finally to irregularly shaped flaws. The normalized volumetric energy density input ultimately affects the melting, fluid flow, and solidification process during laser–material interaction. As the energy density increases, the powder bed becomes excessively molten and subsequent vaporization of the material results in a cavity filled with vapor or plasma [37]. Upon solidification, collapse of the keyhole melt pools proceeds when the aggressive vapor pressure is lower than ambient pressures [38]. Consequently, at very high energy density, rapidly solidifying walls prevent the vapor-filled cavity from escaping the deep

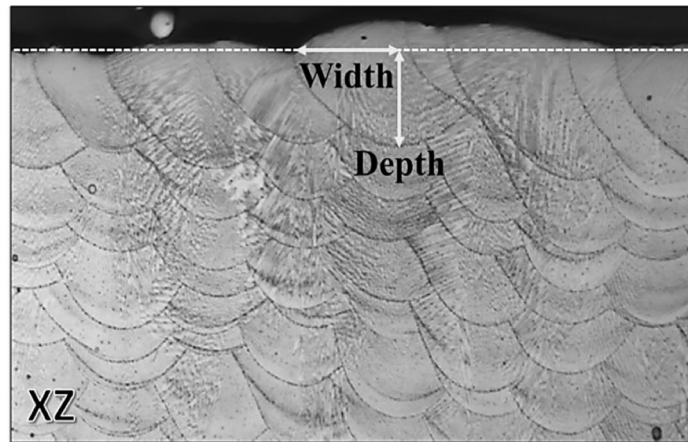
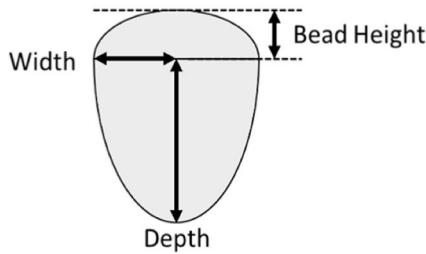


Fig. 1 A schematic and representative optical micrograph of melt pools showing lateral symmetry. Note that the actual melt pool width is twice that of measured width indicated

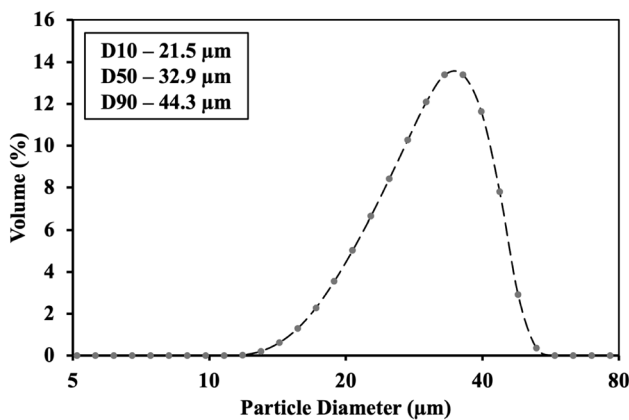


Fig. 2 Particle size distribution of as-received IN718 powder feed-stock

fluctuating keyholes during mechanical collapse [39]. When the laser absorption is insufficient in maintaining the required recoil pressure, the more dominant surface tension driven by the Marangoni effect would keep the liquid surface as small as possible and prevent the occurrence of a keyhole [40]. In direct contrast, a very low energy density resulted in a clear engagement of conduction mode. The powder bed is melted by heat conduction effects at higher laser scan speeds, and the shape of conduction mode melt pools is controlled by thermal conduction [41], which explains the appearance of irregular or lack of fusion defects.

Effect of Laser Power and Scan Speed on Relative Density

All metallurgical flaws were quantified on both XY and XZ cross sections, as presented in Fig. 6. While the average relative density obtained using Archimedes’ method was,

in general, lower than that obtained via image analysis, the overall trend as functions of LPBF parameters remained consistent for both methods of measurements. Samples with the highest relative density were found at moderate scan speeds within their respective laser power and scan speed ranges. For all laser powers examined, the relative density gradually increased to a maximum and then gradually decreased as a function of scan speed.

The relative density is also plotted in Fig. 7 as a function of energy density, as determined by Eq 1. When fused with a laser power of 125 W, the relative density was highest at 57.9 J/mm³ and gradually decreased as energy density increased. This pattern of changing relative density was more clearly observed when fabricated at higher laser powers, e.g., 200 W, 275 W, and 350 W. As illustrated in Fig. 7(b)–(d), the relative density increased sharply before reaching the maximum. The decrease in relative density over an increasing range of energy density appeared to be more gradual at higher laser powers compared to lower laser powers. For all investigated laser powers, the relative density was the highest when energy density employed was between 50 and 100 J/mm³, and this observation is consistent with the literature [42, 43].

A simplistic model was devised to quantitatively correlate the relative density and volumetric energy density. Assuming thermally activated processes of melting and evaporation, exponential functions were defined by:

$$\text{Relative Density} = 100 - A \exp(-b * E_{\rho}^v) - C \exp(d * E_{\rho}^v - f) \tag{2}$$

where *A*, *b*, *C*, *d*, and *f* are constants, and *E*_ρ^v is the volumetric energy density. Constants *A* and *b* approximate the density curve at low energy density where fusion is dependent on the melting behavior of the material. *C*, *d*, and *f* approximate

Fig. 3 (a) Optical micrograph of unetched IN718 powder cross section, (b) secondary electron (SE) micrograph of IN718 powder, (c) backscatter electron (BSE) micrograph of IN718 powder, (d) cellular-dendritic microstructural details in BSE micrograph

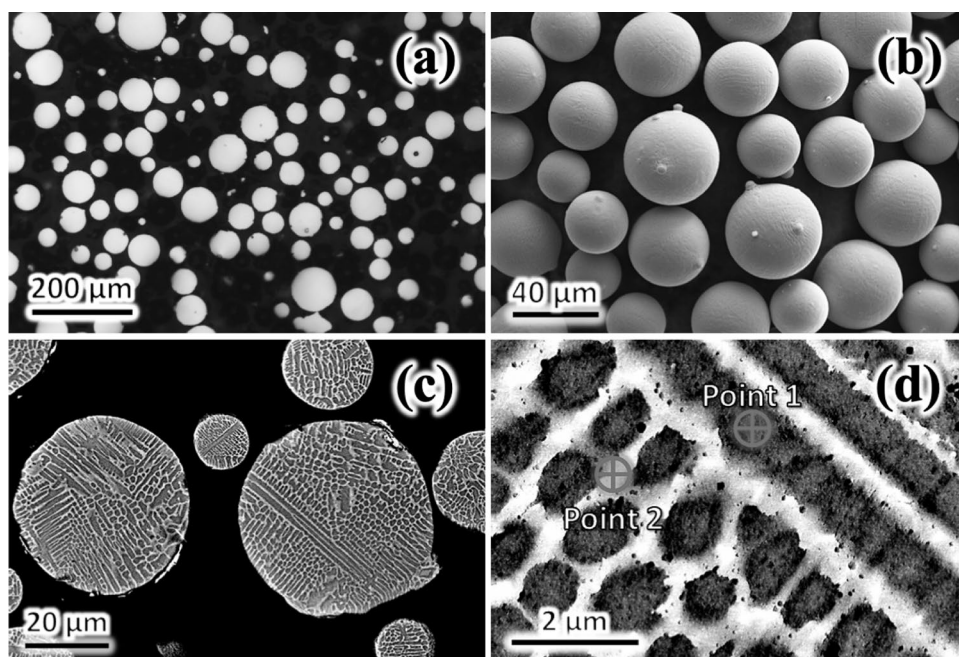


Table 2 EDS composition (wt.%) from regions of interests identified in Fig. 3(d) from IN718 powder feedstock

	Ni	Cr	Fe	Nb	Mo	Co	Ti	Al	Si	Mn
Point 1	51.7 (± 0.5)	19.5 (± 0.2)	18.7 (± 0.2)	7.5 (± 0.3)	1.3 (± 0.2)	...	0.7 (± 0.1)	0.4 (± 0.1)	0.3 (± 0.1)	...
Point 2	48.3 (± 0.5)	18.0 (± 0.2)	15.8 (± 0.2)	14.2 (± 0.3)	1.9 (± 0.3)	0.1 (± 0.1)	1.1 (± 0.1)	0.2 (± 0.1)	0.3 (± 0.1)	...

the density curve at high energy density, where keyhole formation related to evaporation would take place. Figure 8(a) plots the sample relative density with respect to the E_p^v . At first glance, Fig. 8(a) demonstrates a good fit. However, Table 3 outlines the calculated constants as defined by Eq (2), and the corresponding residuals for 5 prediction iterations with nearly constant root-mean-square error (RMSE) at 7.2. While constants A , b , d , and f have relatively low standard deviations, the pre-exponential constant C has a high standard deviation. This indicates some inconsistency between the model and the experimental data. Notice that there are no experimental data below 30.86 J/mm^3 , and this is strictly due to insufficient energy to melt/fuse the powder bed. As such, the model attempted the fit without any experimental data below 30.86 J/mm^3 , or a boundary condition corresponding to zero energy density.

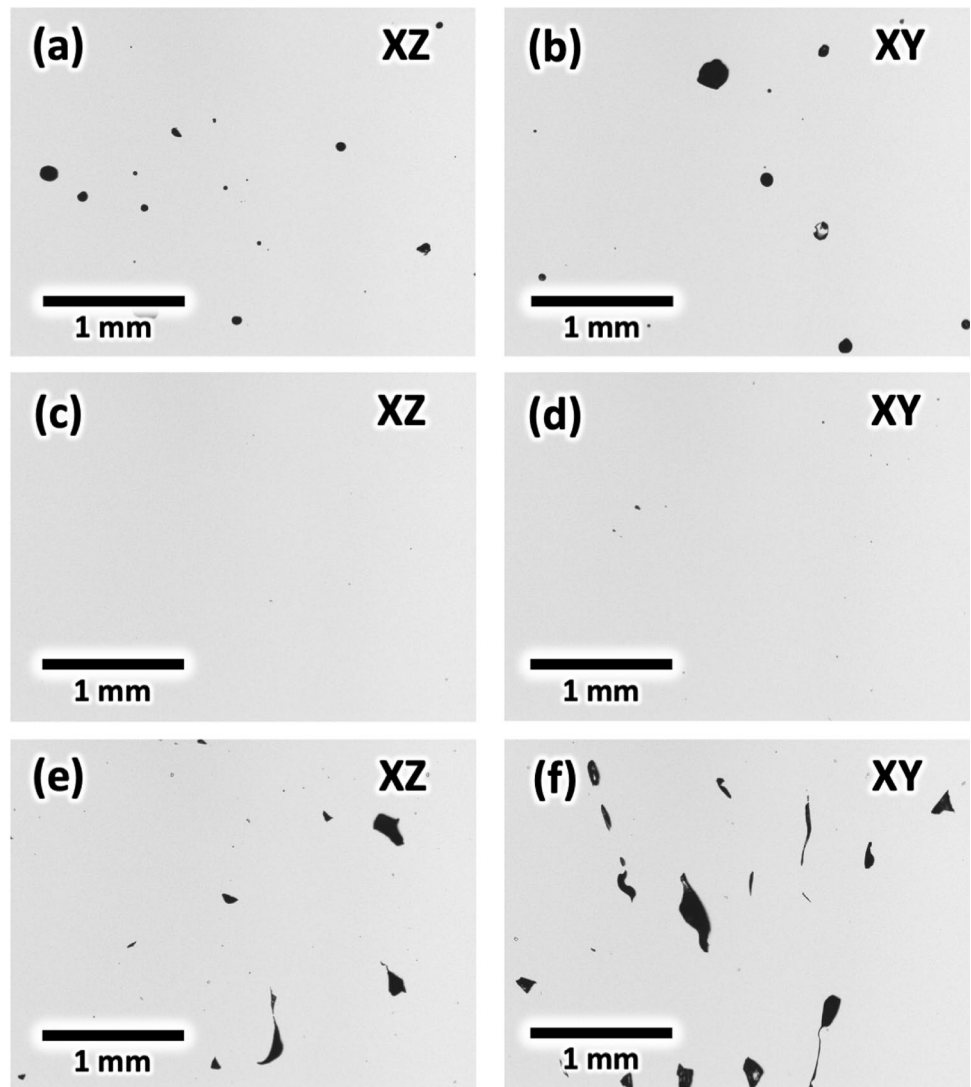
While the perfectly closest packing density of monosized spheres or powders cannot be more than $\pi/(3\sqrt{2}) \approx 0.74$ [44], a narrow Gaussian distribution of powders should have lower packing density. For a narrow particle radii range between 0.67 and 1.5 of the mean, the packing density and coordination number are ~ 0.58 and ~ 5.9 , respectively [45]. Since the IN718 powder feedstock particle radii range between ~ 0.33 and ~ 1.76 of the mean, the theoretical

packing density should be no higher than 70%. As such, an assumed relative density value of 70% was added at an energy density of zero J/mm^3 . Figure 8(b) shows the curve fit obtained from the model and the experimental data as a function of energy density. Although similar to Fig. 8(a), the additional data point at zero J/mm^3 reduced the standard deviation reported in Table 4, including that for the constant C . A consistent RMSE was approximately 7.3.

Effect of Laser Power and Scan Speed on Microstructure

Figure 9 depicts the typical layer-by-layer microstructure and the melt pool characteristics of IN718 samples produced at constant laser power of 125 W, and varying laser scan speeds. Both the melt pool width and depth decreased with increasing laser scan speed. Figure 9(a) and (b) presents the microstructure of samples produced with high energy density, in which deep keyhole melt pools solidified producing spherical keyhole pores. By increasing laser scan speed to 600 mm/s and 800 mm/s, as presented in Figure 7(c) and (d), respectively, a clear decrease in porosity was observed. A decrease in melt pool dimensions is reflective of the engagement in conduction mode

Fig. 4 Optical micrographs from IN718 exhibiting (a, b) keyhole pores, (c, d) full density and (e, f) lack of fusion flaws from the (a, c, e) XZ and (b, d, f) XY cross sections. These samples fabricated with varying laser scan speed, while power (275 W) hatch spacing (120 μm) and slice thickness (30 μm) were kept constant



during laser–material interaction. This trend in decreasing melt pool dimensions as a function of laser scan speed was consistent for all laser powers examined in this study.

Rosenthal’s equation [46] can be employed as a simple analytical expression to estimate the melt pool development over a wide range of laser powers and scan speeds as described below:

$$T = T_o + \frac{Q}{2\pi Rk} \exp\left(\frac{-v(\xi + R)}{2\alpha}\right) \tag{3}$$

where T is the final temperature, T_o is the build plate temperature, P is the laser power, k is thermal conductivity [47], v is laser scan speed, $R = (\xi^2 + y^2 + z^2)^{1/2}$ is the radial distance from the center of the laser beam, α is the thermal diffusivity, ξ is the distance along the beam travel direction, y is the distance parallel to the build plate, and z is the distance parallel to the build direction.

The predicted melt pool dimensions and experimentally measured dimensions are presented in Fig. 10. The calculated melt pool width corroborates well to the experimental measurement and clearly depicts a gradual decrease over an increasing range of laser scan speeds at a constant laser power. However, melt pool depths calculated using Rosenthal’s equation underestimated the experimental ones, especially for those fabricated with high energy input, up to 350 %. As the laser scan speed increased, the predicted melt pool depths were more comparable to the experimental results.

At slow scan speeds, i.e., high energy densities, the magnitude of the measured melt pool depth was much higher than the measured melt pool width. This trend was more prevalent for higher laser powers—indicative of keyhole mode. An engagement in conduction mode at higher laser scan speeds beyond the high energy density threshold

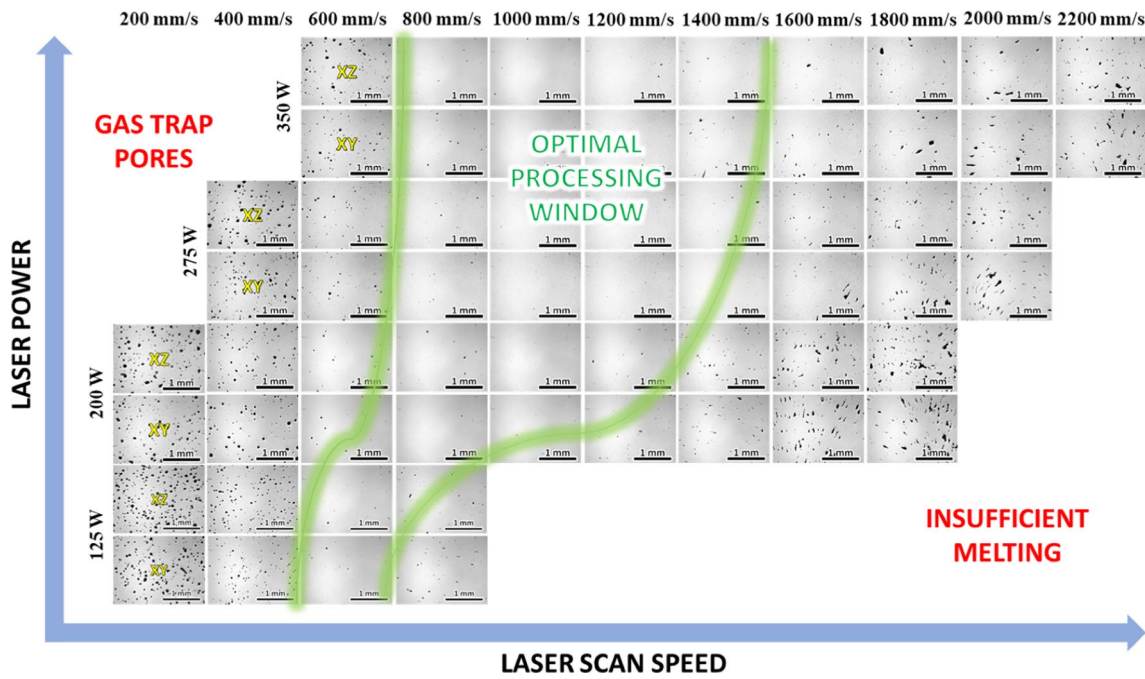


Fig. 5 Optical micrographs of XZ and XY cross sections of IN718 samples produced with varying laser power and laser scan speed, while hatch spacing (120 μm) and slice thickness (30 μm) were kept constant

Fig. 6 Relative sample density as a function of laser scan speeds at constant hatch spacing and slice thickness of 120 μm and 30 μm, respectively, for laser power of (a) 125 W; (b) 200 W; (c) 275 W; and (d) 350 W

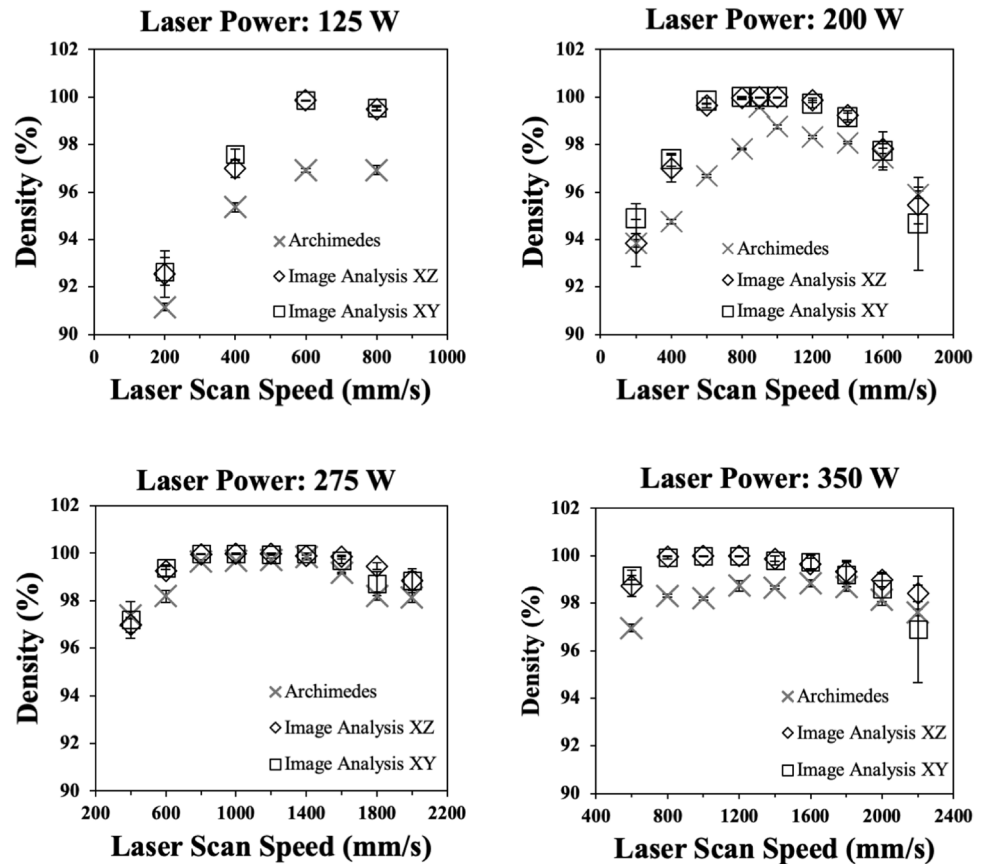


Fig. 7 Relative sample density as a function of energy density at hatch spacing, slice thickness, and scan rotation angle of 120 μm , 30 μm , and 16°, respectively, for laser power of (a) 125 W; (b) 200 W; (c) 275 W; and (d) 350 W

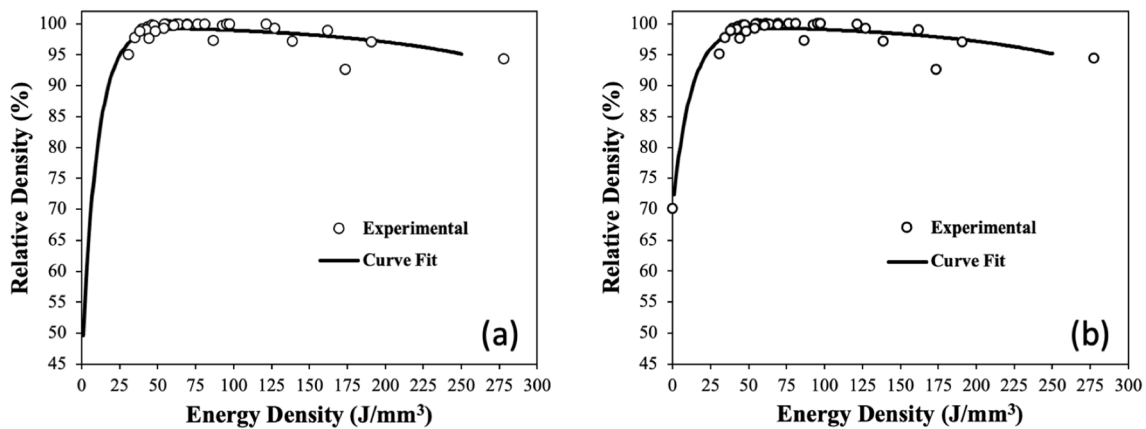
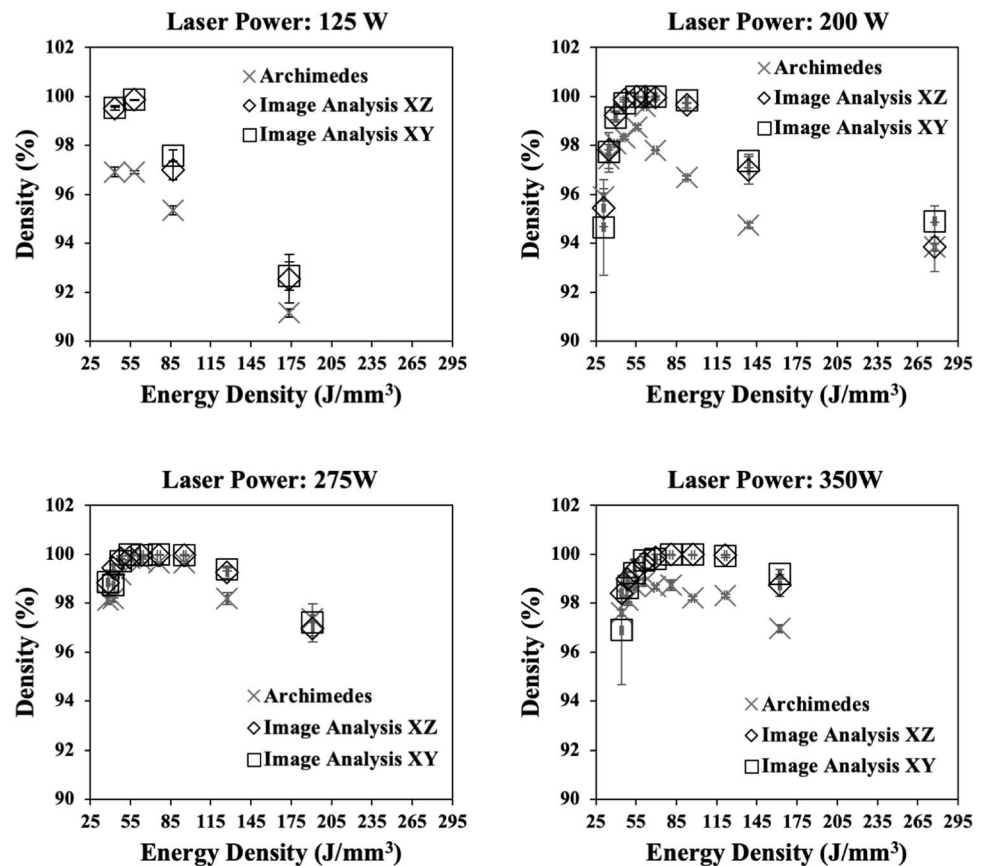


Fig. 8 Predicted and experimental relative densities as a function of energy density (a) without and (b) with density (e.g., powder packing) of 70 % corresponding to zero energy density

produced shallower melt pools. Samples fabricated at 125 W exhibited a more gradual decrease in melt pool depth compared to the steep decrease observed with higher laser powers. Since the Rosenthal equation yields the predicted temperature both at and below the interacting surface, combinations of ξ , y , and z , in which the temperature reaches the liquidus temperature will provide estimates of the melt

pool size and shape. Thus, unstable keyholes with significant internal temperature variation and dynamic fluid flow [48] need to be incorporated into the model in order to correctly predict the formation of melt pool depth at high energy density [49–54].

Figure 11 presents typical microstructure of IN718 sample produced by LPBF with overlapping consecutive melt

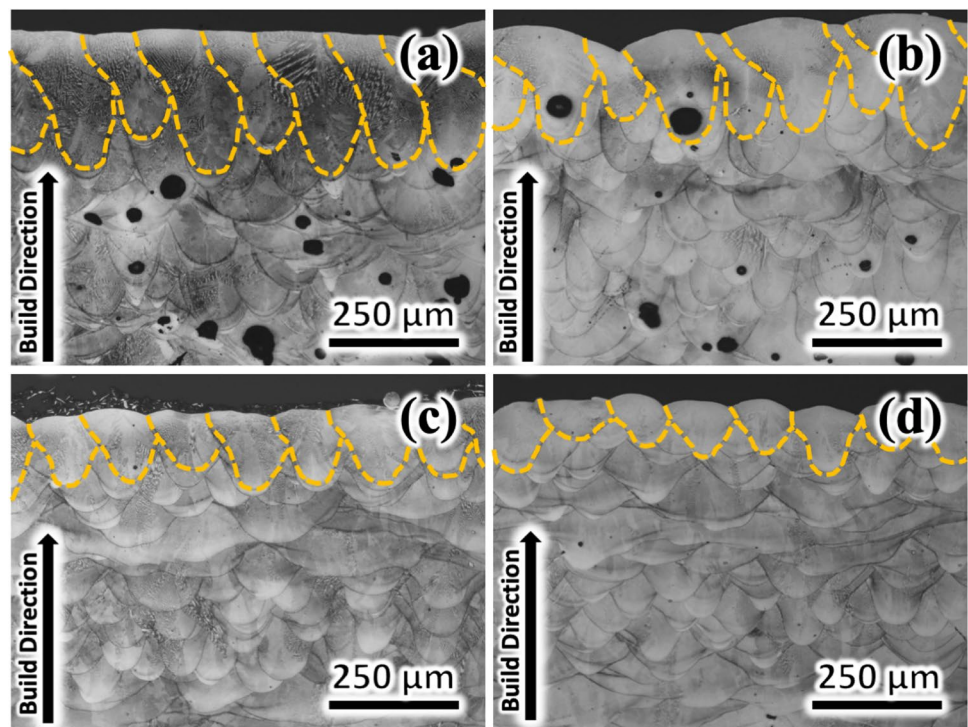
Table 3 Calculated constants without artificial relative density point

Iteration	A	b (mm^3/J)	C	d (mm^3/J)	f	RMSE
1	58.24468	0.10136	10.20256	0.00999	3.29402	7.20753
2	54.37903	0.10059	11.27128	0.01003	3.40288	7.21968
3	52.08941	0.09667	19.76539	0.01028	4.02188	7.21910
4	52.36739	0.09656	18.45234	0.01025	3.94879	7.22158
5	58.94424	0.10135	21.88401	0.01025	4.11260	7.18741
Average (SD)	55.20495 (3.22733)	0.09931 (0.00248)	16.31511 (5.25092)	0.01016 (0.00014)	3.75603 (0.03785)	7.21106 (0.01433)

Table 4 Calculated constants with artificial relative density point

Iteration	A	b (mm^3/J)	C	d (mm^3/J)	f	RMSE
1	29.75860	0.08421	2.22715	0.01099	1.98692	7.32819
2	29.75435	0.08434	1.56237	0.01095	1.61892	7.32851
3	29.76189	0.08409	2.40009	0.01105	2.07363	7.32804
4	29.75306	0.08442	1.71224	0.01091	1.70366	7.32879
5	29.75328	0.08429	2.05710	0.01097	1.90092	7.32832
Average (SD)	29.75622 (0.00384)	0.08427 (0.00013)	1.99179 (0.34961)	0.01097 (0.00005)	1.85679 (0.19098)	7.32837 (0.00029)

Fig. 9 Melt pools observed parallel to the build direction at scan speeds of: (a) 200 mm/s, (b) 400 mm/s, (c) 600 mm/s, (d) 800 mm/s. Laser power, hatch spacing, slice thickness, and scan rotation angle were constant at 125W, 120 μm , 30 μm , and 16°, respectively

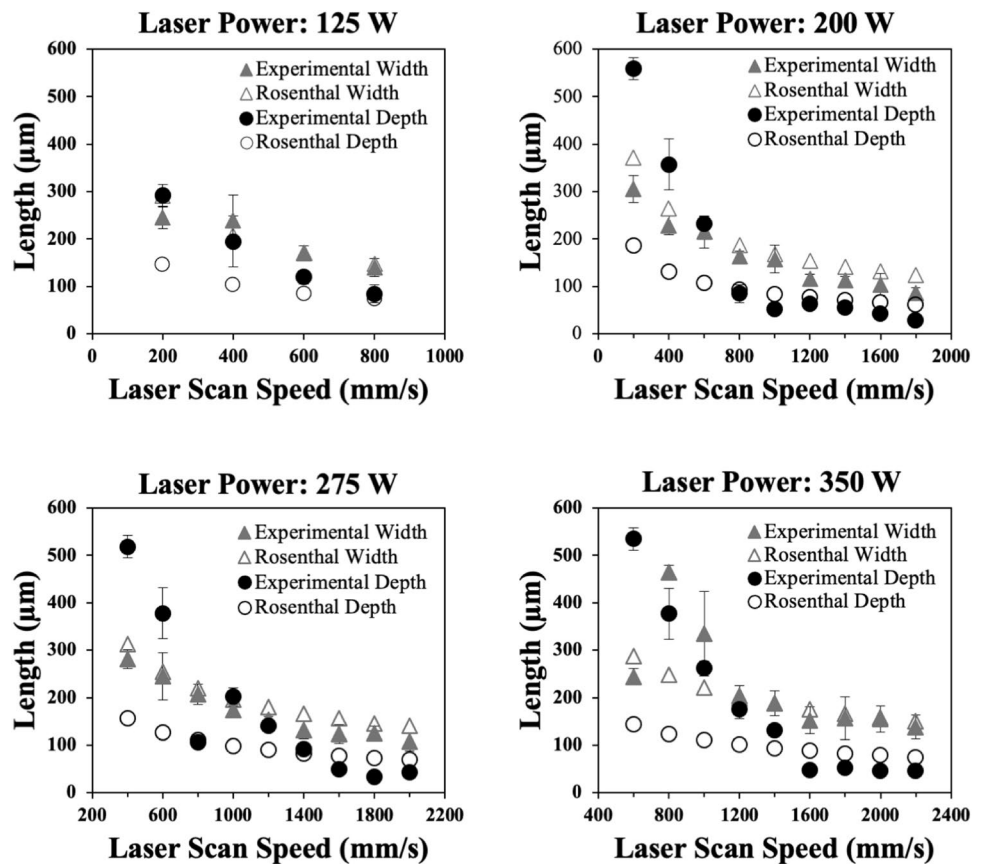


pools generated by the layer-by-layer fusion process. This is common when viewing parallel to the build direction, i.e., XZ cross section as shown in Fig. 11(a). Figure 11(b) presents overlapping melt pools as a network of discontinuous and multidirectional laser tracks in the XY cross section based on scan rotation angle. BSE micrograph in Fig. 11(c) depicts melt pool boundaries, equiaxed cells and elongated

dendritic microstructure in the XZ cross section. The XY cross section shown by the high magnification BSE micrograph, presented in Fig. 11(d), revealed a more equiaxed cellular network.

Due to the invariability and equiaxed cellular network found in the XY cross sections, quantification of the cell size was conducted only using micrographs taken from the XY

Fig. 10 Melt pool dimensions experimentally measured and predicted by Rosenthal’s equation as a function of laser scan speed at constant hatch spacing, slice thickness, and scan rotation angle of 120 μm, 30 μm, and 16°, respectively, for laser power of (a) 125 W; (b) 200 W; (c) 275 W; and (d) 350 W



plane. Figure 12 illustrates the change in the average cell size as a function of laser scan speeds at different laser powers. As scan speed increased, the average cell size decreased. In other words, reduction in energy density corresponds to the reduction in average cell size, and this trend was consistent for all laser powers investigated in this study.

The cooling rate can be correlated with the measured cell size. A phenomenological method that relates the secondary dendrite arm spacing (SDAS) to the cooling rate was employed, in which the measured cellular spacing was used in lieu of the SDAS. The cooling rate was approximated using the following expression [55]:

$$\lambda = m\dot{T}^{-n} \tag{4}$$

where λ is the cellular spacing, \dot{T} is the cooling rate, and m and n are materials constants, equal to 50 and 0.33, respectively, for IN718 [56].

In addition, Rosenthal’s equation describes the change in temperature of a moving point heat source, which can be employed to estimate the change in temperature of a moving laser at a specified laser scan speed. Thus, the cooling rate \dot{T} of each sample was also estimated using Rosenthal’s

equation to illustrate the trend of cooling rates as a function of laser scan speeds. A simplified Rosenthal solution [57] used to determine the cooling rates is expressed by:

$$\dot{T} = 2\pi k(T_s - T_o)(T_L - T_o) \frac{v}{PA} \tag{5}$$

where k is the thermal conductivity, T_s is the solidus temperature, T_o is the build plate temperature, T_L is the liquidus temperature, v is the laser scan speed, P is the laser power, and A is the laser absorption coefficient. Equation (4) assumes constant average thermal properties such as thermal conductivity and laser absorptivity; however, this is not the case in LPBF. Based on highspeed imaging [11], the powder bed melts within a few microseconds; therefore, calculations were carried out using materials constants at both the room temperature and the liquidus temperature to distinguish the difference in the trend of the cooling rates. The thermal conductivity of IN718 used in Eq (4) at room temperature and liquidus temperature is 11.4 W/m·K and 26.7 W/m·K, respectively [47, 58]. The laser absorptivity of IN718 at room temperature and liquidus temperature is 0.62 and 0.07, respectively [49].

Fig. 11 Optical micrographs of SLMed IN718 obtained (a) parallel to the build direction and (b) perpendicular to the build direction. Backscatter electron micrographs of SLMed IN718 (c) parallel to the build direction and (d) perpendicular to the build direction. Laser power, laser scan speed, hatch spacing, slice thickness, and scan rotation angle were constant at 125 W, 800 mm/s, 120 μm , 30 μm , and 16°, respectively

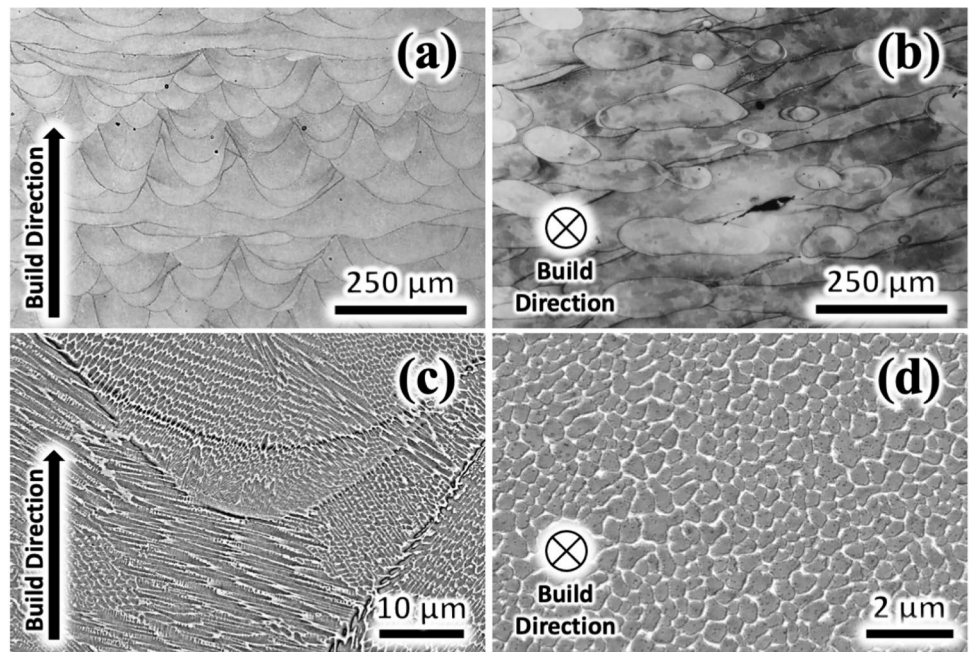


Fig. 12 Variation in average cell size as a function of laser scan speed. Laser power, hatch spacing, slice thickness, and scan rotation angle were held constant at 125 W, 120 μm , 30 μm , and 16°, respectively, for laser power of (a) 125 W; (b) 200 W; (c) 275 W; and (d) 350 W

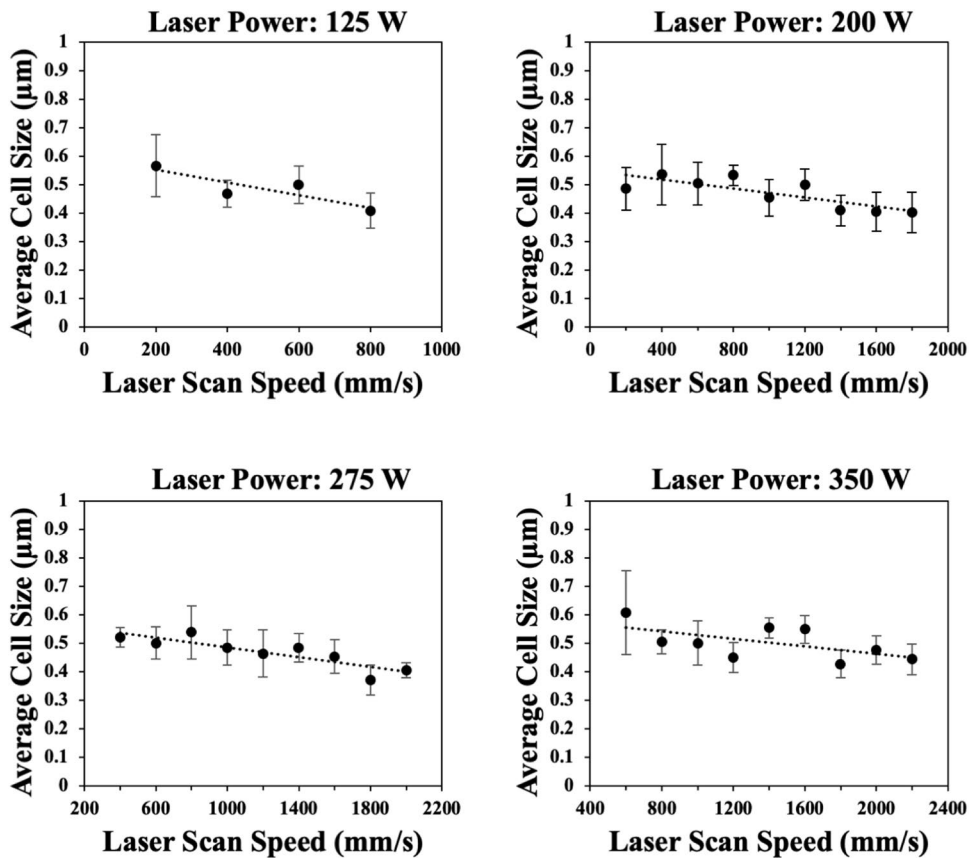


Fig. 13 Comparison between SDAS and Rosenthal cooling rates at varying laser powers and scan speeds at constant hatch spacing, slice thickness, and scan rotation angle of 120 μm , 30 μm , and 16 $^\circ$, respectively, for laser power of (a) 125 W; (b) 200 W; (c) 275 W; and (d) 350 W

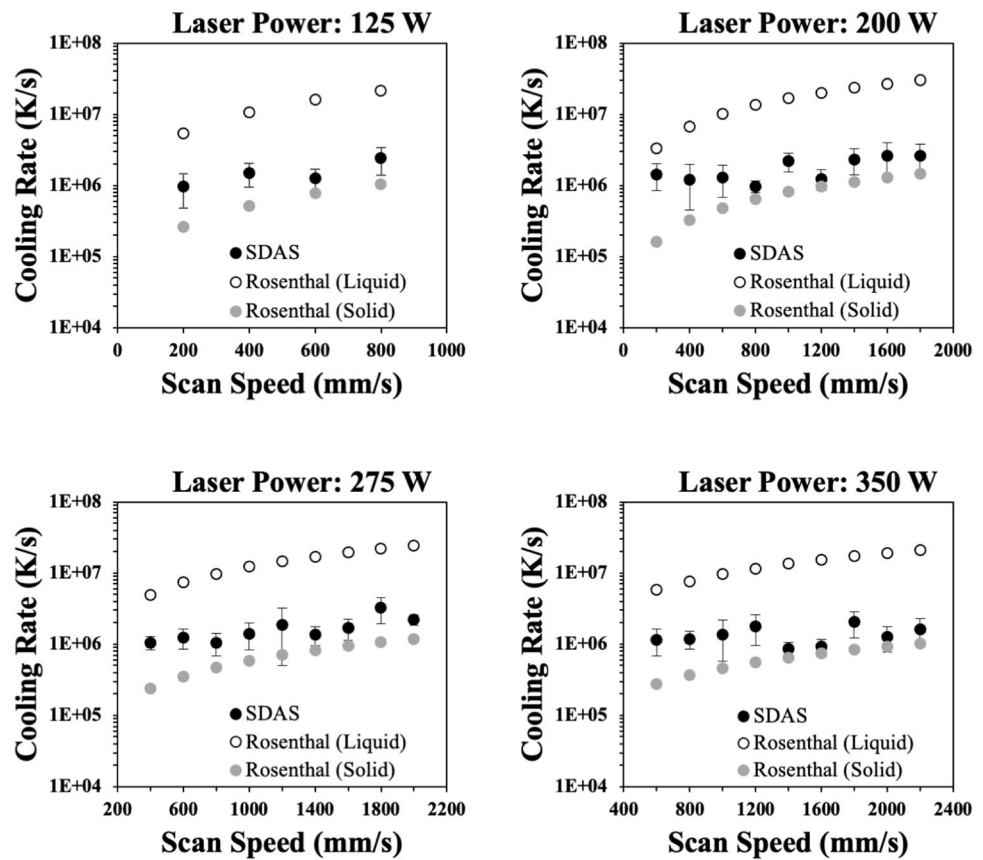


Figure 12 presents cooling rates estimated by using thermal properties of IN718 at the liquidus temperature, i.e., Rosenthal (liquid) and at room temperature, i.e., Rosenthal (solid). The measured cellular spacing assumed as SDAS yielded cooling rates in the range of 10⁶ K/s for all processing parameters examined. Cooling rates estimated based on Rosenthal’s equation using room temperature thermal properties were in the order of 10⁵ K/s to 10⁶ K/s. The cooling rates calculated using Rosenthal’s equation with thermal conductivity and laser absorptivity of the liquid phase yielded cooling rates in the order of 10⁶ to 10⁷ K/s. In general, the estimated cooling rates increased as the laser scan speed increased, which corroborated well to the decreasing cell size observed with faster laser scan speeds as shown in Fig. 11. Moreover, the cooling rate determined from the measured cell size lied between the estimate by Rosenthal’s equation with liquidus and solid (room temperature) properties.

The SDAS is an important characteristic in solidification microstructure because it is related to the diffusion distance in the solidification process and directly influences

the microsegregation. The simple model proposed by Katamis *et al.* [55] was used to predict the final SDAS based on coarsening mechanism. Since the cell size was used in place of the secondary dendrite arm, the approximated cooling rate can only provide a semiempirical relationship between the cooling rate and the laser scan speed at constant power. Nonetheless, the estimated values obtained from Eq (3) are quite consistent with numerically simulated values for the SLM process [59]. Although the estimated cooling rates from the Rosenthal equation used constant thermophysical properties of IN718 at the liquidus or room temperature, the trend and magnitude were comparable to those estimated from the measurement of cell size. Since the use of Eq (4) relies on thermophysical constants, estimated values can only illustrate the trend of cooling rates over a range of laser scan speed (Fig. 13).

Effect of Laser Scan Rotation Angle

To examine the influence of laser scan rotation angle on the relative density: laser scan speed, hatch spacing, and slice

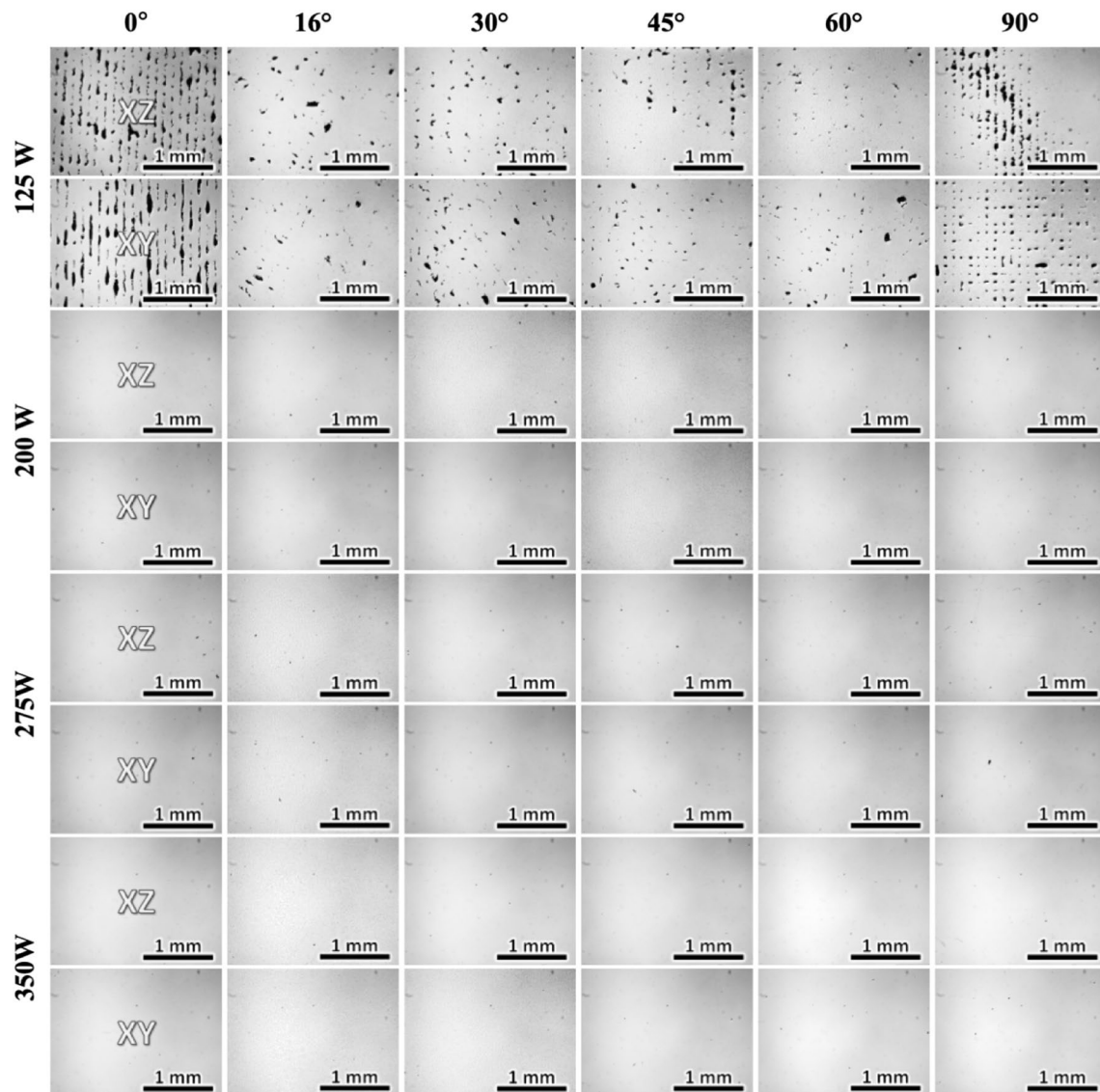


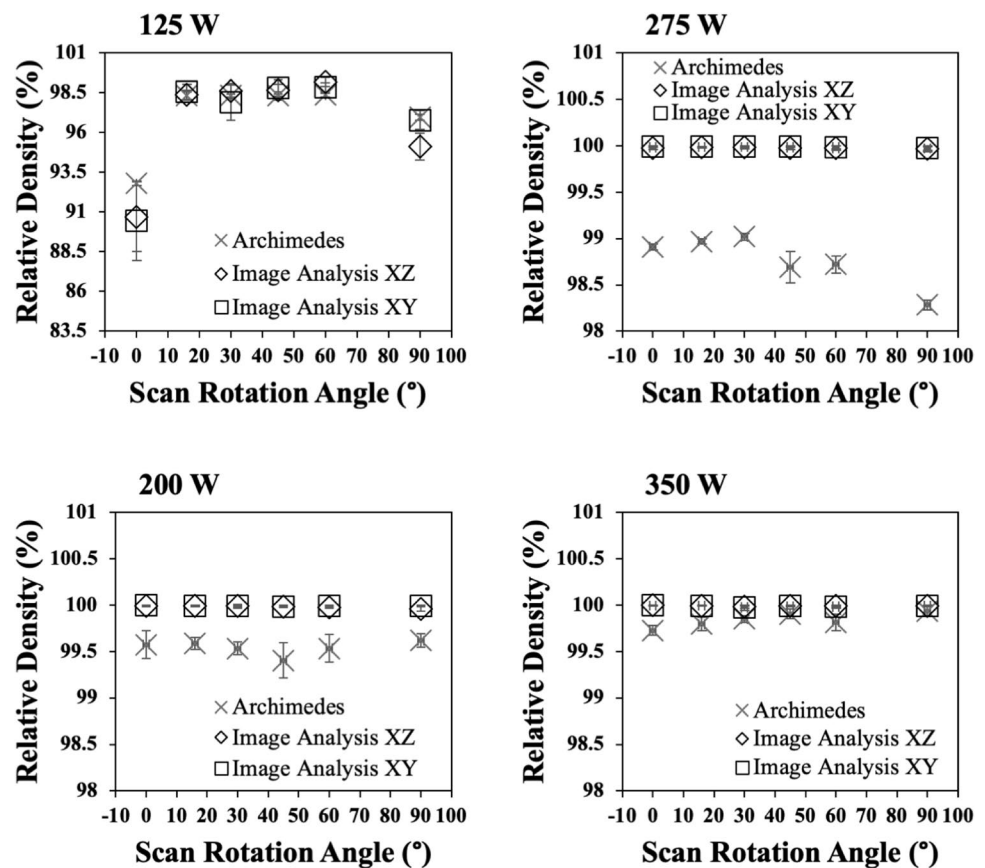
Fig. 14 Optical micrographs from IN718 samples produced as functions of laser power and scan rotation angle. The other parameters, laser scan speed, hatch spacing, and slice thickness were kept constant at 900 mm/s, 120 μ m, 30 μ m, respectively

thickness were kept constant at 900 mm/s, 120 μ m, 30 μ m, respectively. As depicted in Fig. 14, when fused with 200 W or higher, the variation in laser scan rotation angle had minimal influence on the overall part density. However, samples fused with 125 W had significant differences in defect formation. The unidirectional scanning (0 degrees) produced a semi-continuous pattern of flaws across the XZ and XY cross sections. At an angle rotation of 16 degrees, the semi-continuous network of defects was replaced by sparsely distributed flaws. At scan rotation angles of 30, 45, and 60

degrees, some amounts of networked flaws were observed. Increasing the scan rotation angle to 90 degrees produced a grid-like pattern of flaws from alternating layers of laser tracks.

Figure 15 plots the relative density of IN718 samples as a function of laser scan rotation angles for various laser powers. The relative density of specimens fabricated at 125 W using scan rotation strategies of 0° and 90° resulted in low relative densities of ~ 90% and ~ 96%, respectively. In contrast, the relative densities of samples fabricated at 16°, 30°,

Fig. 15 Relative density as a function of laser scan rotation angles at laser power of (a) 125 W; (b) 200 W; (c) 275 W; and (d) 350 W. Scan speed, hatch spacing, and slice thickness were held constant at 900 mm/s, 120 μm, and 30 μm, respectively



45°, and 60° using 125 W were nearly identical. In general, higher laser powers of 200 W, 275 W and 350 W produced dense samples regardless of scan rotation angle.

Quantification of melt pool dimensions was also obtained for the samples printed as a function of laser scan rotation angle as presented in Fig. 16. No discernable trend in melt pool width and depth was observed as a function of scan rotation angle regardless of laser power employed. Overall, the melt pool widths were larger than the depths, which corresponds to conduction melting mode.

Figure 17 presents the BSE micrographs of equiaxed cellular structures observed perpendicular to the build direction. The equiaxed cellular microstructure in IN718 was produced regardless of laser scan rotation angle and laser power. Figure 18 presents the measured cell size as a function of laser scan rotation angle at each laser power. Using laser power of 125 W and 250 W, the variation in laser scan

rotation angles had minimal effect on the average cell size; except at 125W, the average cell size of sample printed using laser scan rotation of 0 degrees was noticeably larger than those from other scan rotation angles. This phenomenon is most likely due to the poor heat dissipation within the sample during solidification.

To highlight the potential influence of melt pool development and its influence on heat dissipation, i.e., conduction paths, Fig. 19 compares the difference in melt pool development between samples fabricated at constant power, speed, scan rotation and slice thickness, but using different hatch spacings. Figure 19 (a) shows the XZ cross section of the sample without laser scan rotation strategy. Lack of fusion flaws was observed between each laser raster, separated by 120 μm. The inherent voids and free space, such as those shown in Fig. 14 for the laser power of 125 W, would prevent effective conductive heat transfer during the LPBF.

Fig. 16 Melt pool dimensions as a function of laser scan rotation angles at laser power of (a) 125 W; (b) 200 W; (c) 275 W; and (d) 350 W. Scan speed, hatch spacing, and slice thickness were held constant at 900 mm/s, 120 μm , and 30 μm , respectively

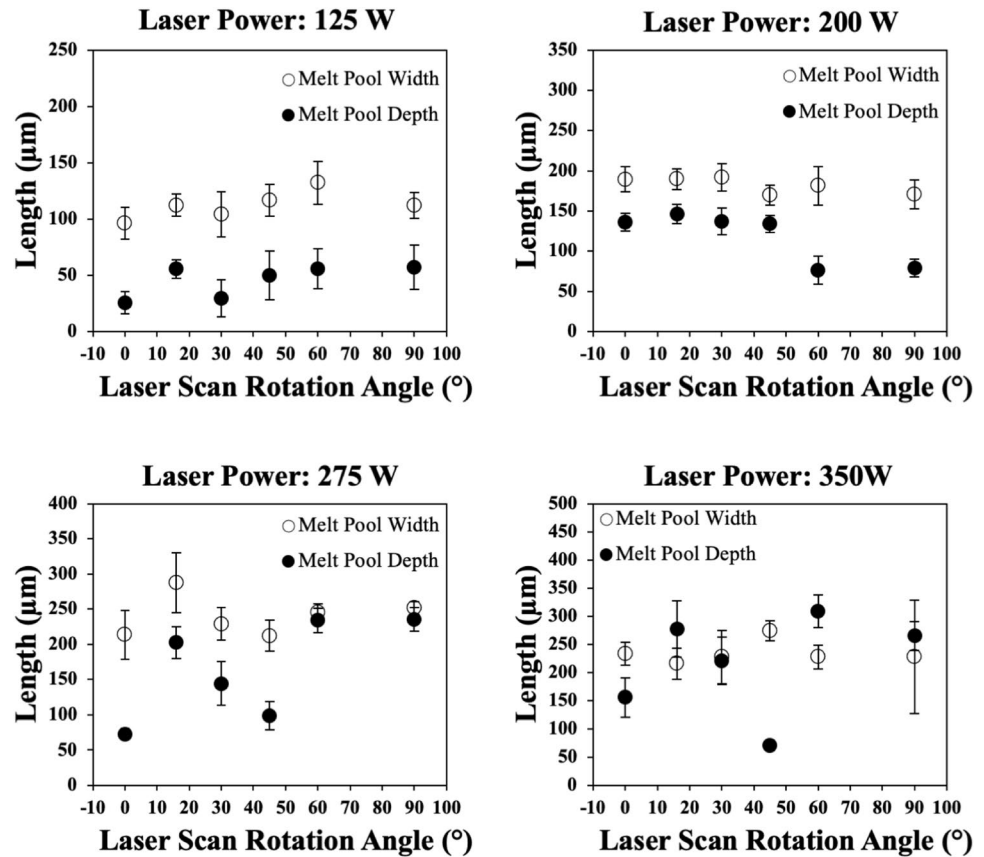
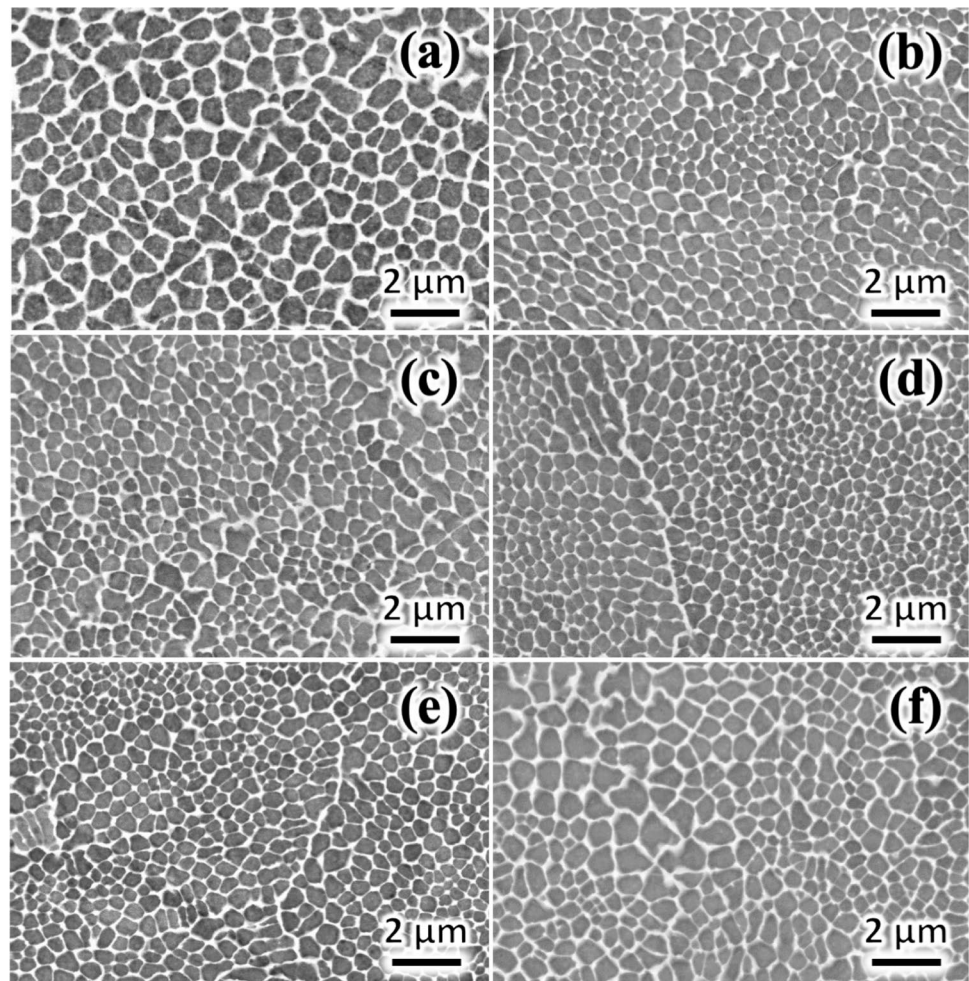


Figure 18(c) and (d) plots the average cell size as a function of laser scan rotation angles at higher laser powers of 275 W and 350 W. The average cell size seemed to vary more as a function of laser scan rotation angles. The relationship between cell size and laser scan speed plotted in Fig. 12 demonstrated that the average cell size can be related to the cooling rate of the melt pool as reported in Fig. 13. Through single laser track studies, Wang et al. [32] compared the solidification behavior between melt pools under conduction and keyhole mode. They observed that the thermal gradient, G , and solidification rate, R , varied within the melt pool. From the bottom to the top, G decreased, and R increased, regardless of melting modes. While the cooling rate, \dot{T} can be related to the cell size in Eq (3), \dot{T} can be further related to G and R in the following relation [60]:

$$\dot{T} = GR \quad (6)$$

Since the scan speed, hatch spacing, and slice thickness were held constant, the energy density is much greater for the samples fabricated at higher laser powers. The higher energy density will produce deeper melt pools, and thus more variation in G and R . Figure 20(a) and (b) compares the melt pool depth of specimens fabricated at 200 W and 350 W, respectively. With the same scan rotation strategy, the sample with the higher energy density has deeper melt pools. High magnification BSE micrographs in Fig. 20(c)–(e) depict the top, middle, and bottom portions, respectively, of the keyhole melt pool shown in Fig. 20(b). These micrographs demonstrate that the cell size can vary at each location within each melt pool. The cell size will vary more, deeper the melt pools, and the variation in cell size at higher laser powers was influenced by the energy density rather than the scan rotation strategy.

Fig. 17 BSE micrographs showing cellular microstructure observed perpendicular to the build direction as a function of laser scan rotation angle of (a) 0°, (b) 16°, (c) 30°, (d) 45°, (e) 60°, and (f) 90°. Laser power, scan speed, hatch spacing, and slice thickness were held constant at 125 W, 900 mm/s, 120 μm , and 30 μm , respectively



Concluding Remarks

Effect of LPBF parameters such as laser power, laser scan speed, and laser scan rotation angle was systematically investigated to examine the solidification microstructure development of IN718. Optimal processing windows were observed for all laser powers examined in this study. At low laser power, e.g., 125 W, the optimal processing window was small and a more abrupt transition from circular pores to irregular flaws was observed. At higher laser powers, optimal processing window was enlarged, and the transition from circular porosity to irregular flaws was more gradual. In general,

the laser scan rotation strategy had minimal influence on the relative density and the cell size, except at 125 W.

Relative density higher than 99.5% was observed when samples were fabricated with energy density within the range of 50 and 100 J/mm^3 . The laser–material interaction at low laser scan speeds produced keyhole melt pools with depths much greater than the half width. At moderate laser scan speeds, the optimal processing zone, melt pools had a mixed combination of keyhole and conduction melting. At high laser scan speeds, development of conduction melt pools was observed. Estimated melt pool width by Rosenthal's equation corroborated well to measured melt pool width, however,

Fig. 18 Average cell size as a function of laser scan rotation angles at laser power of (a) 125 W; (b) 200 W; (c) 275 W; and (d) 350 W. Scan speed, hatch spacing, and slice thickness were held constant at 900 mm/s, 120 μm , and 30 μm , respectively

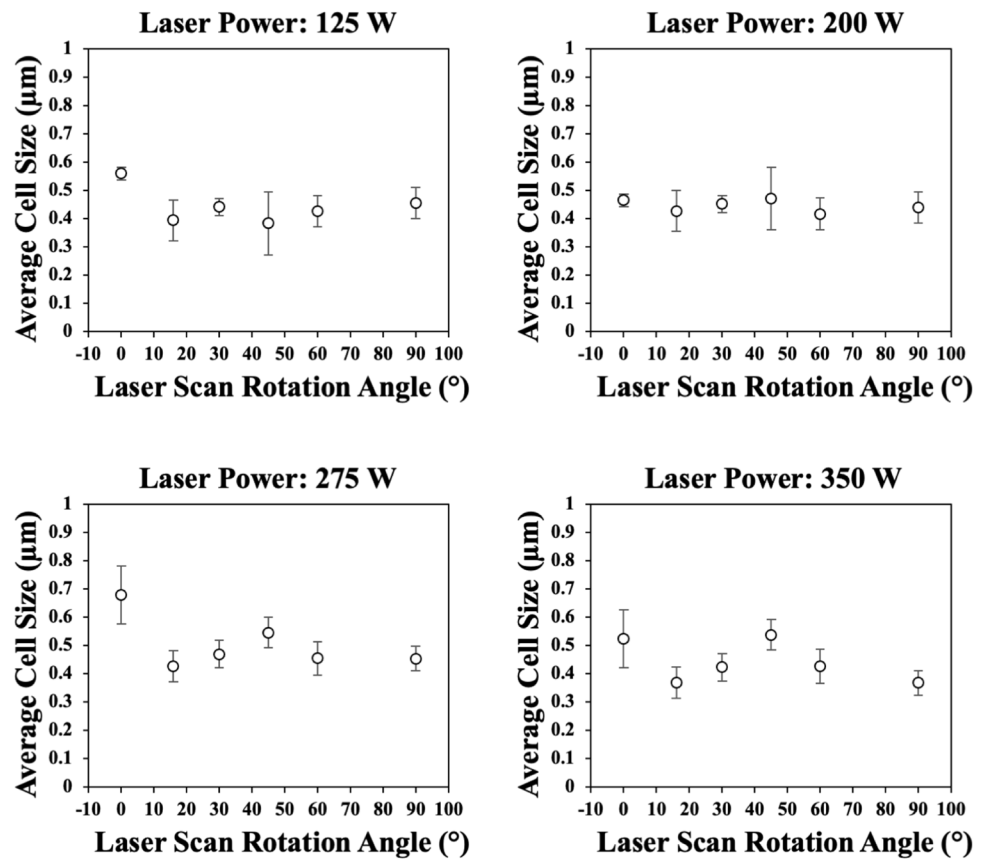
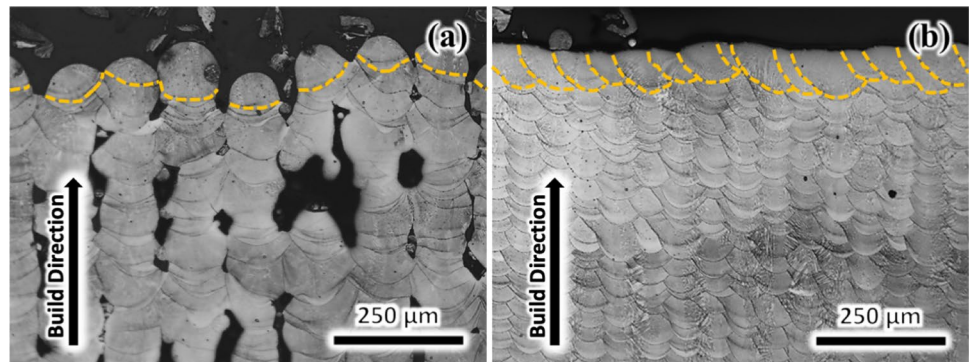


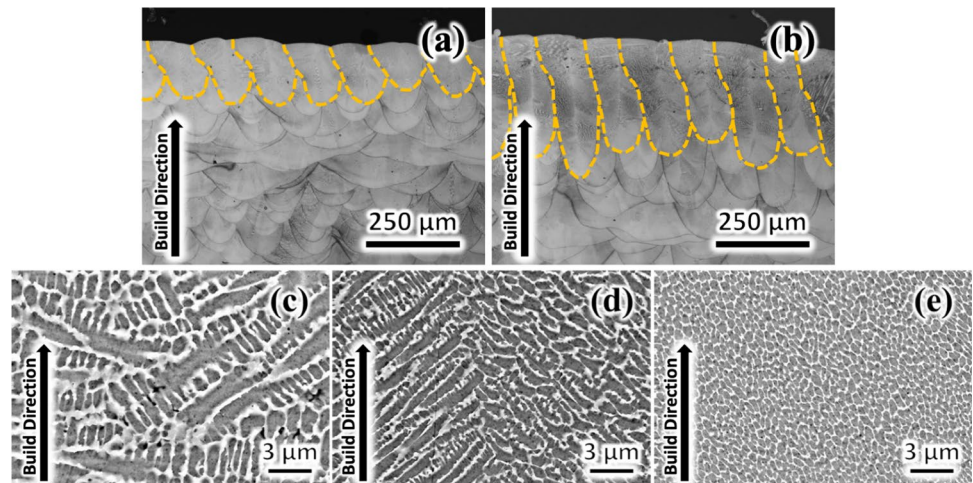
Fig. 19 Optical micrographs of XZ cross section with laser power, scan speed, and slice thickness of 125 W, 900 mm/s, 30 μm , respectively, at hatch spacing: (a) 120 μm , (b) 60 μm



the melt pool depth estimation underestimated the experimental results, particularly when the energy density was high and keyhole mode was prevalent. A simple empirical model was employed to correlate relative sample density and LPBF volumetric energy density with an assumption of two thermally activated processes, i.e., melting and evaporation.

Quantification of the cellular microstructure indicated that there is a decrease in the cellular spacing as the laser scan speed increased at constant power. The cooling rates increased with an increase in laser scan speed. Cooling rates estimated by both the cell size measurement and Rosenthal's equation were in the order of 10^5 to 10^7 K/s.

Fig. 20 Melt pool comparison between (a) 200 W and (b) 350 W at scan rotation angle, scan speed, hatch spacing, and slice thickness of 16° , 900 mm/s, 120 μm , and 30 μm , respectively. The cell size within deep melt pools observed in (b): (c) near melt pool surface, (d) middle of melt pool, (e) near the bottom of melt pool



Acknowledgements This research was sponsored by the Battelle Energy Alliances, LLC under a contract, No. DE-AC07-05ID14517-214376 with collaboration from authors of Idaho National Laboratory. The views, opinions and conclusions made in this document are those of the authors and should not be interpreted as representing the official policies, either expressed or implied, of the Battelle Energy Alliances or Idaho National Laboratory or the U.S. Government. The U.S. Government is authorized to reproduce and distribute reprints for Government purposes notwithstanding any copyright notation herein.

References

- W.E. King, A.T. Anderson, R.M. Ferencz, N.E. Hodge, C. Kamath, S.A. Khairallah, A.M. Rubenchik, Laser powder bed fusion additive manufacturing of metals; physics, computational, and materials challenges. *Appl. Phys. Rev.* **2**(4), 041304 (2015)
- D. Herzog, V. Seyda, E. Wycisk, C. Emmelmann, Additive manufacturing of metals. *Acta Mater.* **117**, 371–392 (2016)
- M. Lewandowski, V. Sahai, R. Wilcox, C. Matlock, R. Overfelt, High temperature deformation of Inconel 718 castings. *Superalloys*. **718**, 625–706 (1994)
- T.M. Pollock, S. Tin, Nickel-based superalloys for advanced turbine engines: chemistry, microstructure and properties. *J. Propul. Power.* **22**(2), 361–374 (2006)
- W.E. Frazier, Metal additive manufacturing: a review. *J. Mater. Eng. Perform.* **23**(6), 1917–1928 (2014)
- H. Hyer, L. Zhou, Q. Liu, D. Wu, S. Song, Y. Bai, B. McWilliams, K. Cho, Y. Sohn, High strength WE43 microlattice structures additively manufactured by laser powder bed fusion. *Materialia*. **16**, 101067 (2021)
- B. Zheng, Y. Zhou, J.E. Smugeresky, J.M. Schoenung, E.J. Lavernia, Thermal behavior and microstructure evolution during laser deposition with laser-engineered net shaping: part II. Experimental investigation and discussion. *Metall. Mater. Trans. A.* **39**(9), 2237–2245 (2008)
- X. Wang, L.N. Carter, B. Pang, M.M. Attallah, M.H. Loretto, Microstructure and yield strength of SLM-fabricated CM247LC Ni-Superalloy. *Acta Mater.* **128**, 87–95 (2017)
- H. Hyer, L. Zhou, A. Mehta, Y. Sohn, Effects of alloy composition and solid-state diffusion kinetics on powder bed fusion cracking susceptibility. *J. Phase Equilib. Diffus.* **42**(1), 5–13 (2021)
- S. Dadbakhsh, B. Vrancken, J.P. Kruth, J. Luyten, J. Van Humbeeck, Texture and anisotropy in selective laser melting of NiTi alloy. *Mater. Sci. Eng., A.* **650**, 225–232 (2016)
- U.S. Bertoli, G. Guss, S. Wu, M.J. Matthews, J.M. Schoenung, In-situ characterization of laser-powder interaction and cooling rates through high-speed imaging of powder bed fusion additive manufacturing. *Mater. Des.* **135**, 385–396 (2017)
- R. Konečná, G. Nicoletto, L. Kunz, A. Bača, Microstructure and directional fatigue behavior of Inconel 718 produced by selective laser melting. *Procedia Struct. Integr.* **2**, 2381–2388 (2016)
- H. Hyer, L. Zhou, S. Park, T. Huynh, A. Mehta, S. Thapliyal, R.S. Mishra, Y. Sohn, Elimination of extraordinarily high cracking susceptibility of aluminum alloy fabricated by laser powder bed fusion. *J. Mater. Sci. Technol.* **103**, 50–58 (2022)
- L. Zhou, H. Hyer, J. Chang, A. Mehta, T. Huynh, Y. Yang, Y. Sohn, Microstructure, mechanical performance, and corrosion behavior of additively manufactured aluminum alloy 5083 with 0.7 and 1.0 wt.% Zr addition. *Mater. Sci. Eng. A.* **823**, 141679 (2021)
- A. Mehta, L. Zhou, T. Huynh, S. Park, H. Hyer, S. Song, Y. Bai, D.D. Imholte, N.E. Woolstenhulme, D.M. Wachs, Y. Sohn, Additive manufacturing and mechanical properties of the dense and crack free Zr-modified aluminum alloy 6061 fabricated by the laser-powder bed fusion. *Addit. Manuf.* **41**, 101966 (2021)
- H. Hyer, R. Newell, D. Matejczyk, S. Hsie, M. Anthony, L. Zhou, C. Kammerer, Y. Sohn, Microstructural development in as built and heat treated IN625 component additively manufactured by laser powder bed fusion. *J. Phase Equilib. Diffus.* **42**(1), 14–27 (2021)
- R. Seede, B. Zhang, A. Whitt, S. Picak, S. Gibbons, P. Flater, A. Elwany, R. Arroyave, I. Karaman, Effect of heat treatments on the microstructure and mechanical properties of an ultra-high strength martensitic steel fabricated via laser powder bed fusion additive manufacturing. *Addit. Manuf.* **2**, 102255 (2021)
- A. Mahmud, T. Huynh, L. Zhou, H. Hyer, A. Mehta, D.D. Imholte, N.E. Woolstenhulme, D.M. Wachs, Y. Sohn, Mechanical behavior assessment of Ti-6Al-4V ELI alloy produced by laser powder bed fusion. *Metals*. **11**(11), 1671 (2021)
- L. Zhou, T. Huynh, S. Park, H. Hyer, A. Mehta, S. Song, Y. Bai, B. McWilliams, K. Cho, Y. Sohn, Laser powder bed fusion of Al-10 wt.% Ce alloys: microstructure and tensile property. *J. Mater. Sci.* **55**(29), 14611–14625 (2020)
- S. Kou, A criterion for cracking during solidification. *Acta Mater.* **88**, 366–374 (2015)
- S. Kou, Solidification and liquation cracking issues in welding. *JOM*. **55**(6), 37–42 (2003)

22. M.C. Flemings, Solidification processing. *Metall. Mater. Trans. B.* **5**(10), 2121–2134 (1974)
23. R.J. Vikram, A. Singh, S. Suwas, Effect of heat treatment on the modification of microstructure of selective laser melted (SLM) IN718 and its consequences on mechanical behavior. *J. Mater. Res.* **35**(15), 1949–1962 (2020)
24. J. Lee, M. Lee, Correlation between microstructure and tensile properties of STS 316L and inconel 718 fabricated by selective laser melting (SLM). *J. Nanosci. Nanotechnol.* **20**, 6807–6814 (2020)
25. E. Chlebus, K. Gruber, B. Kuźnicka, J. Kurzac, T. Kurzynowski, Effect of heat treatment on the microstructure and mechanical properties of Inconel 718 processed by selective laser melting. *Mater. Sci. Eng. A.* **639**, 647–655 (2015)
26. X. Wang, P.W. Liu, Y. Ji, Y. Liu, M.H. Horstemeyer, L. Chen, Investigation on microsegregation of IN718 alloy during additive manufacturing via integrated phase-field and finite-element modeling. *J. Mater. Eng. Perform.* **28**(2), 657–665 (2019)
27. L. Zhou, A. Mehta, B. McWilliams, K. Cho, Y. Sohn, Microstructure, precipitates and mechanical properties of powder bed fused inconel 718 before and after heat treatment. *J. Mater. Sci. Technol.* **35**(6), 1153–1164 (2019)
28. J.J. Schirra, R.H. Caless, R.W. Hatala, The effect of the Laves phase on the mechanical properties of wrought and cast + HIP Inconel 718. *Miner. Metals Mater. Soc.* **42**, 375–388 (2012)
29. S.A. Mantri, S. Dasari, A. Sharma, T. Alam, M.V. Pantawane, M. Pole, S. Sharma, N.B. Dahotre, R. Banerjee, S. Banerjee, Effect of micro-segregation of alloying elements on the precipitation behaviour in laser surface engineered Alloy 718. *Acta Mater.* **210**, 116844 (2021)
30. D. Zhang, P. Zhang, Z. Liu, Z. Feng, C. Wang, Y. Guo, Thermo-fluid field of molten pool and its effects during selective laser melting (SLM) of Inconel 718 alloy. *Addit. Manuf.* **21**, 567–578 (2018)
31. W.E. King, H.D. Barth, V.M. Castillo, G.F. Gallegos, J.W. Gibbs, D.E. Hahn, C. Kamath, A.M. Rubenchik, Observation of keyhole-mode laser melting in laser powder-bed fusion additive manufacturing. *J. Mater. Process. Technol.* **214**(12), 2915–2925 (2014)
32. H. Wang, L. Wang, R. Cui, B. Wang, L. Luo, Y. Su, Differences in microstructure and nano-hardness of selective laser melted Inconel 718 single tracks under various melting modes of molten pool. *J. Market. Res.* **9**(5), 10401–10410 (2020)
33. G.A. Rao, M. Kumar, M. Srinivas, D.S. Sarma, Effect of standard heat treatment on the microstructure and mechanical properties of hot isostatically pressed superalloy inconel 718. *Mater. Sci. Eng. A.* **355**(1–2), 114–125 (2003)
34. K.N. Amato, S.M. Gaytan, L.E. Murr, E. Martinez, P.W. Shindo, J. Hernandez, S. Collins, F. Medina, Microstructures and mechanical behavior of Inconel 718 fabricated by selective laser melting. *Acta Mater.* **60**(5), 2229–2239 (2012)
35. D. Zhang, Z. Feng, C. Wang, W. Wang, Z. Liu, W. Niu, Comparison of microstructures and mechanical properties of Inconel 718 alloy processed by selective laser melting and casting. *Mater. Sci. Eng. A.* **724**, 357–367 (2018)
36. T.G. Gallmeyer, S. Moorthy, B.B. Kappes, M.J. Mills, B. Amin-Ahmadi, A.P. Stebner, Knowledge of process-structure-property relationships to engineer better heat treatments for laser powder bed fusion additive manufactured Inconel 718. *Addit. Manuf.* **31**, 100977 (2020)
37. P. Mohanty, J. Mazumder, Solidification behavior and microstructural evolution during laser beam—material interaction. *Metall. Mater. Trans. B.* **29**(6), 1269–1279 (1998)
38. J. Kroos, U. Gratzke, M. Vicanek, G. Simon, Dynamic behaviour of the keyhole in laser welding. *J. Phys. D Appl. Phys.* **26**, 481–486 (1992)
39. A. Matsunawa, J.-D. Kim, N. Seto, M. Mizutani, S. Katayama, Dynamics of keyhole and molten pool in laser welding. *J. Laser Appl.* **10**(6), 247–254 (1998)
40. H. Zhao, W. Niu, B. Zhang, Y. Lei, M. Kodama, T. Ishide, Modelling of keyhole dynamics and porosity formation considering the adaptive keyhole shape and three-phase coupling during deep-penetration laser welding. *J. Phys. D Appl. Phys.* **44**, 10239 (2011)
41. T. Qi, H. Zhu, H. Zhang, J. Yin, L. Ke, X. Zeng, Selective laser melting of Al7050 powder: Melting mode transition and comparison of the characteristics between the keyhole and conduction mode. *Mater. Des.* **135**, 257–266 (2017)
42. G.V.L. De Noe, L.I. Perez-Andrade, J. Corona-Castuera, D.G. Espinosa-Arbelaez, J. Muñoz-Saldaña, J.M. Alvarado-Orozco, Study of volumetric energy density limitations on the IN718 mesostructure and microstructure in laser powder bed fusion process. *J. Manuf. Process.* **64**, 1261–1272 (2021)
43. H. Hyer, L. Zhou, S. Park, G. Gottsfriz, G. Benson, B. Tolentino, B. McWilliams, K. Cho, Y. Sohn, Understanding the laser powder bed fusion of AlSi10Mg alloy. *Metall. Microstruct. Anal.* **9**(4), 484–502 (2020)
44. T. Abu-Lebdeh, R. Damptey, V. Lamberti, S. Hamoush, Powder packing density and its impact on SLM-based additive manufacturing. *Miner. Metals Mater. Soc.* **23**, 355–367 (2019)
45. Y. Shi, Y. Zhang, Simulation of random packing of spherical particles with different size distributions. *Appl. Phys. A.* **92**(3), 621–626 (2008)
46. D. Rosenthal, The theory of moving source of heat and its application to metal treatment. *Trans. ASME.* **43**(11), 849–866 (1946)
47. J. Sweet, E. Roth, M. Moss, Thermal conductivity of Inconel 718 and 304 stainless steel. *Int. J. Thermophys.* **8**(5), 593–606 (1987)
48. H. Ki, J. Mazumder, P.S. Mohanty, Modeling of laser keyhole welding: part II. Simulation of keyhole evolution, velocity, temperature profile, and experimental verification. *Metall. Mater. Trans. A.* **33**(6), 1831–1842 (2002)
49. T.-N. Le, Y.-L. Lo, Z.-H. Lin, Numerical simulation and experimental validation of melting and solidification process in selective laser melting of IN718 alloy. *Addit. Manuf.* **36**, 101519 (2020)
50. C.-C. Tseng, C.-J. Li, Numerical investigation of interfacial dynamics for the melt pool of Ti-6Al-4V powders under a selective laser. *Int. J. Heat Mass Transf.* **134**, 906–919 (2019)
51. S.A. Khairallah, A. Anderson, Mesoscopic simulation model of selective laser melting of stainless steel powder. *J. Mater. Process. Technol.* **214**(11), 2627–2636 (2014)
52. W. Yan, W. Ge, Y. Qian, S. Lin, B. Zhou, W.K. Liu, F. Lin, G.J. Wagner, Multi-physics modeling of single/multiple-track defect mechanisms in electron beam selective melting. *Acta Mater.* **134**, 324–333 (2017)
53. M. Bayat, S. Mohanty, J.H. Hattel, Multiphysics modelling of lack-of-fusion voids formation and evolution in IN718 made by multi-track/multi-layer L-PBF. *Int. J. Heat Mass Transf.* **139**, 95–114 (2019)
54. H.J. Willy, X. Li, Z. Chen, T.S. Herng, S. Chang, C.Y.A. Ong, C. Li, J. Ding, Model of laser energy absorption adjusted to optical measurements with effective use in finite element simulation of selective laser melting. *Mater. Des.* **157**, 24–34 (2018)
55. T.Z. Kattamis, J.M. Coughlin, M.C. Flemings, Influence of coarsening on dendrite arm spacing of aluminum copper alloys. *Trans. ASME.* **239**, 1504 (1967)
56. L. Ling, Y. Han, W. Zhou, H. Gao, D. Shu, J. Wang, M. Kang, B. Sun, Study of microsegregation and Laves phase in Inconel718 superalloy regarding cooling rate during solidification. *Metall. Mater. Trans. A.* **46**(1), 354–361 (2015)
57. M. Tang, P.C. Pistorius, S. Narra, J.L. Beuth, Rapid solidification: selective laser melting of AlSi10Mg. *JOM.* **68**(3), 960–966 (2016)

58. G. Pottlacher, H. Hosaeus, E. Kaschnitz, A. Seifert, Thermophysical properties of solid and liquid Inconel 718 alloy. *Scand. J. Metall.* **31**(3), 161–168 (2002)
59. T. Vilaro, C. Colin, J.-D. Bartout, L. Nazé, M. Sennour, Microstructural and mechanical approaches of the selective laser melting process applied to a nickel-base superalloy. *Mater. Sci. Eng. A.* **534**, 446–451 (2012)
60. S. Kou, *Welding metallurgy*, 3rd edn (Wiley, New York, 2020)

Publisher's Note Springer Nature remains neutral with regard to jurisdictional claims in published maps and institutional affiliations.